Chemical Engineering Science 327 (2026) 123635

Contents lists available at ScienceDirect

Chemical Engineering Science

journal homepage: www.elsevier.com/locate/ces

Ultrahigh SO_2 selective absorption in SO_2/CO_2 mixtures via reversible solid–liquid phase transition in tunable ionic liquids

Xiao-Ya Wang [a,1], Wen-Qiang Gong [b,1], Fei-Feng Mao [a], Wei Hui [a,c,*], Xian-Lu Wu [a], Tiao Zhang [a], Yan Zhou [a], Jia-Yin Zhang [a], Duan-Jian Tao [a,*]

[a] School of Chemical Engineering, Key Laboratory of Functional Small Molecules for Ministry of Education, Jiangxi Normal University, Nanchang, Jiangxi 330022, China
[b] School of Chemistry and Food Science, Nanchang Normal University, Nanchang, Jiangxi 330032, China
[c] School of Life Science, Key Laboratory of Jiangxi Province for Functional Biology and Pollution Control in Red Soil Regions, Jinggangshan University, Ji'an, Jiangxi 343009, China

ARTICLE INFO

Keywords:
Ionic liquids
Sulfur dioxide
Phasetransitionabsorption
DFT
COSMOtherm

ABSTRACT

The high-purity separation of gases with similar properties (e.g., SO_2 *vs.* CO_2) remains a major challenge for ionic liquid (IL) absorbents. In this work, we report the highly efficient and selective capture of SO_2 via SO_2-triggered reversible solid–liquid phase transition in a series of tunable alkyl quaternary ammonium hydrogen sulfate ionic liquids (AQA-HSO_4). The results show that AQA-HSO_4 achieve ultrahigh IAST SO_2/CO_2 selectivities (up to 855) and high uptake capacity (7.1 mmol g^{-1}) at 293.2 K and 100 kPa. This superior performance is rooted in a rationally designed phase transition mechanism, where the modulation of alkyl chain lengths (from ethyl to hexyl) finely tunes the ionic microenvironment by balancing electron-donating and steric effects. Systematic investigations, including SO_2 absorption and kinetic analyses, in-situ FT-IR, DFT and COSMOtherm calculations, reveal that the $[HSO_4]^-$ anion serves as the primary active site, forming suitable cooperative hydrogen bonding and Coulombic interactions specifically with SO_2, while remaining inert to CO_2/N_2. Kinetic analysis confirms that the spontaneous phase transition of AQA-HSO_4 drastically lowers the mass transfer energy barrier, enabling $[N_{4444}][HSO_4]$ to reach 67% of its saturation capacity within 5 min. Additionally, $[N_{4444}][HSO_4]$ exhibits outstanding stability and recyclability, with negligible capacity loss (<0.1%) after 20 absorption–desorption cycles, and can be fully regenerated under mild, energy-efficient conditions (depressurization to ~20 kPa) without external heating. This work provides a promising strategy for developing next-generation, phase-transition-responsive absorbents for high-purity gas separation processes.

1. Introduction

Sulfur dioxide (SO_2), an inevitable byproduct of fossil fuel utilization, is a major contributor to serious environmental problems such as acid rain and $PM_{2.5}$ particles, which pose substantial threats to ecosystems and to human health.(Li et al. 2022; Bora et al., 2025; Tian et al. 2025) In addition, SO_2 is also an indispensable sulfur feedstock with significant application value in medicine, agriculture and other chemical industries. For example, the reduction of high-purity SO_2 to sulfur via the Kraus process provides a fundamental precursor for the synthesis of sulfonamide pharmaceuticals, sulfur-containing agrochemicals, and other high-value fine chemicals.(Ma et al. 2018; Qian et al. 2020) However, the achievement of effective high-purity SO_2 separation remains subject to interference from competing gases, among which CO_2 is an unavoidable competitor.(Deng, Han, and Jiang 2015; Cui et al. 2019) Therefore, developing separation technologies to enable the preferential capture of SO_2 from mixed gases is essential for resource valorization and sustainable development.

In recent years, various SO_2 separation systems have been developed to overcome the limitations of irreversible absorption, solid waste generation, and secondary pollution associated with traditional SO_2 recovery technologies, such as limestone scrubbing, aqueous amine scrubbing, and organic solvent absorption.(Wu et al. 2016; Córdoba 2015; Xie et al. 2024) Among them, ionic liquids (ILs) are regarded as holy grail materials in gas separation engineering and have attracted extensive attention for reversible SO_2 capture owing to their tunable

* Corresponding authors.
E-mail addresses: weihuichem@126.com (W. Hui), djtao@jxnu.edu.cn (D.-J. Tao).
[1] These authors contributed equally to this work.

https://doi.org/10.1016/j.ces.2026.123635
Received 4 January 2026; Received in revised form 8 February 2026; Accepted 15 February 2026
Available online 16 February 2026

structures, negligible vapor pressure, and excellent thermal stability. Many ILs systems have been reported, encompassing guanidinium-, imidazolium-, pyridinium-, phosphonium-, piperazinium-, ammonium-, and hydroxylammonium-based cations, paired with diverse anions such as thiocyanate, nitrile-functionalized species, phenolates, nonprotic heterocycles, and carboxylates.(Qi et al. 2019; Wu et al. 2004; Yang et al. 2013; Wang et al. 2011) However, the difficulty of separating high-purity SO_2 from SO_2/CO_2 mixtures arises from the fact that both gases possess acidic properties and similar kinetic diameters ($SO_2 \approx 4.11$ Å, $CO_2 \approx 3.30$ Å), and show overlapping physicochemical absorption behaviors in many IL systems. For example, Lei and co-workers reported that the solubilities of SO_2 and CO_2 in ILs (e.g., [BMIM][BF_4]) at room-temperature are of the same order of magnitude, whereas that of N_2 is 2–3 orders of magnitude lower.(Lei, Dai, and Chen 2014) Although strong chemical interactions between ILs and SO_2 can afford high uptake capacities and favorable absorption enthalpies, such interactions inevitably lead to substantial energy consumption during absorbent regeneration. Conversely, strategies aimed at weakening IL-SO_2 interactions to reduce the desorption energy generally result in a concomitant decrease in absorption capacity and selectivity. Therefore, achieving efficient and highly selective SO_2 separation remains an unresolved challenge.

In fact, previous studies have demonstrated that employing ILs with low pKa values (<4) is an effective strategy to enhance SO_2/CO_2 separation selectivity. For example, pyridinium-based absorbents containing acidic [SCN] anions afforded an SO_2/CO_2 selectivity of up to 79.(Zeng et al. 2015) Similarly, cyano-containing protic ILs ([DMPANH][MOAc] and [DMAPNH][EOAc]) have superior SO_2/CO_2 selectivity of 119 and 107, respectively.(Zhang et al. 2016) In the field of CO_2 separation, phase transition absorption has attracted significant attention for CO_2 capture due to its ability to yield high-purity products. However, investigations focusing on phase-transition absorption of single-component SO_2 remain relatively scarce. Earlier studies primarily utilized mixtures of SO_2 absorbents with paraffin or high-boiling-point solvents (e.g., DABCO, DMEE) to achieve phase stratification upon SO_2 uptake.(Xu et al. 2019; Zhao et al. 2017) Nevertheless, these systems involve the formation of solid products during SO_2 absorption, which leads to blockages in equipment and pipelines.

To avoid problems arising from the solid phase, some studies have turned to liquid–liquid phase-transition for SO_2 separation. For example, Heldebrant et al. employed N,N-dibutylundecylamine as the absorbent and n-decane as the solvent to achieve liquid–liquid phase transition after SO_2 absorption, but regeneration of this mixed system required vacuum conditions at 70 °C.(Heldebrant, Koech, and Yonker 2010) Subsequently, Zhao et al. utilized the monoamine N,N-dimethylcyclohexylamine (DMCHA) as the absorbent, with high-boiling liquid paraffin (LP) as the solvent to suppress volatility, thereby increasing the molar selectivity of SO_2/CO_2 to 440. However, the capacity loss of DMCHA + LP remained a significant issue, as 29.4% of SO_2 could not be released even after desorption at 100 °C.(Li et al. 2018) Therefore, the design of novel single-component SO_2 absorbents with high selectivity and mild recovery properties holds important application value for high-purity SO_2 recovery.

Herein, we designed and synthesized a series of alkyl quaternary ammonium bisulfate ionic liquids (AQA-HSO_4) for SO_2 separation. The absorption performances (SO_2, CO_2 and N_2) of these AQA-HSO_4 ILs were evaluated to elucidate how the electron-donating and steric effects of different alkyl chains modulate phase-transition behavior and separation efficiency. The results demonstrate that SO_2-triggered solid–liquid phase transition behavior of AQA-HSO_4 ILs during SO_2 absorption can be controlled by modulating the cationic alkyl chain length. Meanwhile, the phase transition is triggered only by SO_2 rather than competitive gases (CO_2 and N_2), which confer ultra-high IAST SO_2/CO_2 selectivity to AQA-HSO_4 ILs. In addition, kinetic and diffusion models were employed to analyze the differences between gas–solid film diffusion, intra-IL diffusion, and final equilibrium. Furthermore, the phase-transition and molecular interaction mechanisms were elucidated through a combination of in-situ FT-IR, DFT, and COSMOtherm calculations. Additionally, the long-term stability and energy-efficient regeneration conditions of these ILs were verified through rigorous absorption–desorption cyclic experiments.

2. Experimental

2.1. Materials

Tetraethylammonium hydroxide solution ([N_{2222}][OH], 40% in water) and tetrabutylammonium hydroxide solution ([N_{4444}][OH], 25% in water) were produced by Shanghai Energy Chemical Reagent Co., Ltd. Tetrahexylammonium bromide ([N_{6666}]Br, 99%) and anion exchange resin (Amberlite 717) were purchased from Shanghai Aladdin Chemical Reagent Co., Ltd. Sulfuric acid (H_2SO_4, 98%) and ethanol (CH_3CH_2OH, AR) were obtained from Tianjin Fuchen Chemical Reagent Co., Ltd. Sulfur dioxide (SO_2, 99.999%) and carbon dioxide (CO_2, 99.999%) were supplied by Jiangxi Huahong Special Gases Co., Ltd. In addition, the other reagents were obtained commercially and used directly without any purification.

2.2. Synthesis and characterization

In this work, alkyl quaternary ammonium-based hydrogen sulfate ionic liquids (AQA-HSO_4 ILs) were synthesized by neutralization, and the structures are shown in Fig. 1a (inset). In a typical synthesis of tetrabutylammonium hydrogen sulfate ILs ([N_{4444}][HSO_4]), equimolar amounts of [N_{4444}][OH] and H_2SO_4 were mixed and stirred at room temperature for 6 h. After completion, the solvent was removed using a rotary evaporator to afford the crude product, which was subsequently vacuum dried at 353 K for 24 h to obtain white solid [N_{4444}][HSO_4]. For tetrahexylammonium hydrogen sulfate ([N_{6666}][HSO_4]), the corresponding tetra-hexyl-ammonium hydroxide ([N_{6666}][OH]) was prepared from [N_{6666}][Br] via anion-exchange using Amberlite 717 resin, while the subsequent neutralization and purification steps were identical to those described above for [N_{4444}][HSO_4]. The structures of AQA-HSO_4 ILs were confirmed by ^{1}H NMR and ^{13}C NMR spectra (DPX400 MHz, Bruker). The thermal stabilities of AQA-HSO_4 ILs were assessed via thermogravimetric analysis (TGA4000, PerkinElmer) under N_2 atmosphere with a heating rate of 5 K min^{-1} from 273.2 K to 1073.2 K. Magnification sample images of AQA-HSO_4 ILs before and after absorption of SO_2 were obtained by the polarization microscope (WYP-63C-2000MS, Hongsen Weiye Technology). Besides, melting points of the three ILs were determined using a melting-point apparatus (SGWX-4B, Jinke), Fourier-transform infrared (FT-IR) spectra were recorded on a NEXUS 870 (ThermoFisher) spectrometer with KBr as background, and in-situ FT-IR spectra were obtained by Nicolet iS50 (ThermoFisher) spectrometer.

2.3. SO_2 and CO_2 absorption

The dynamic and static absorption tests of gases (SO_2, CO_2 and N_2) by AQA-HSO_4 ILs were examined using dual-chamber volumetric apparatus (Fig. S1) in accordance with the absorption method used in our previous work.(Chen et al. 2025; Fang et al. 2025) Detailed descriptions of the apparatus configuration and operating parameters are provided in Supporting Information S1. For SO_2 absorption–desorption tests, the SO_2-loaded AQA-HSO_4 ILs samples were depressurized to ~20 kPa for 2 h or vacuum for 0.5 h at absorbent temperatures. The regenerated ILs were then reused directly in the next SO_2 uptake experiments to evaluate their reusability under repeated absorption–desorption cycles.

2.4. Computational details

The structures of SO_2 and AQA-HSO_4 ILs molecules were optimized

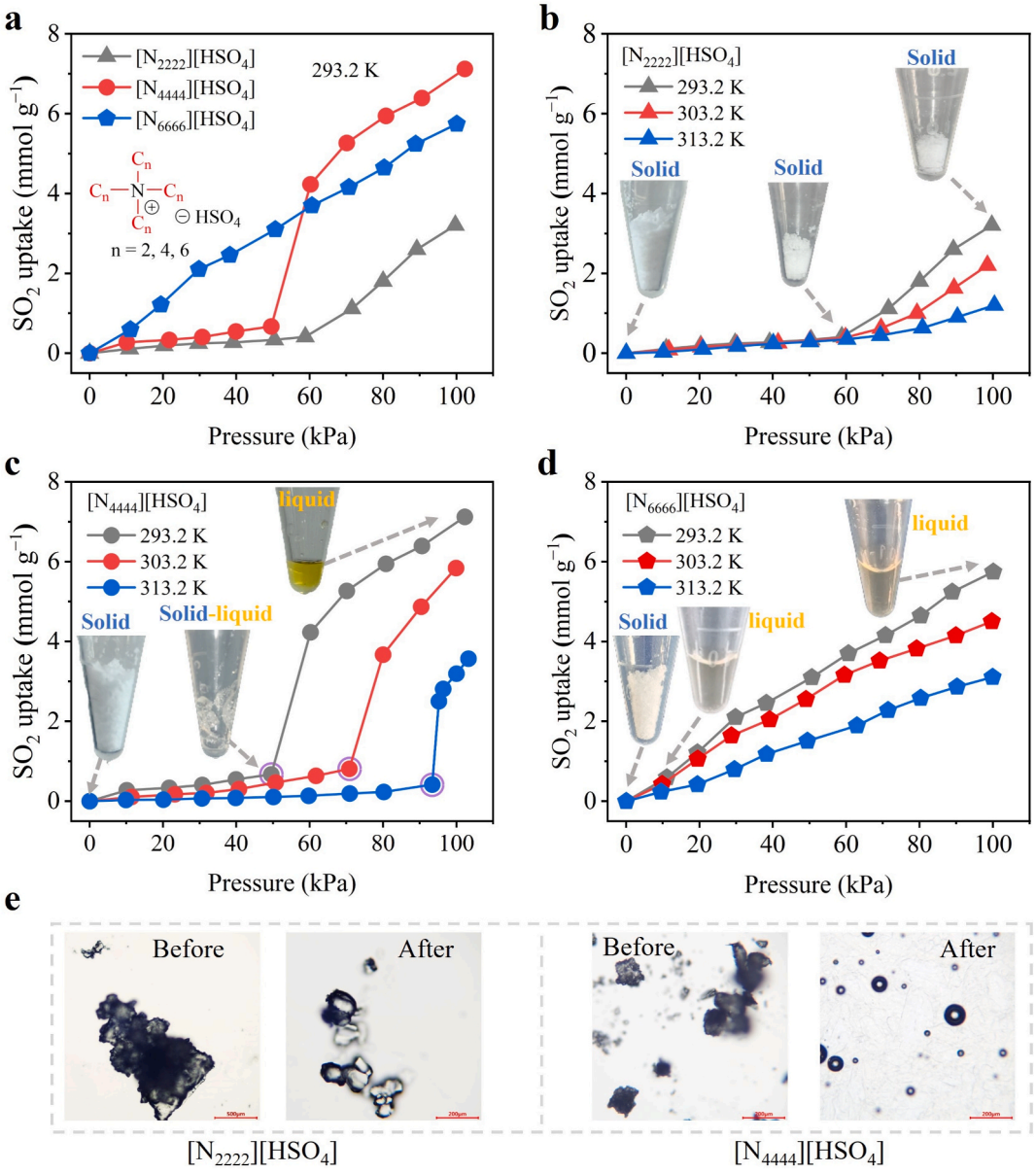

Fig. 1. (a) The SO_2 absorption isotherms of AQA-HSO_4 ILs at 100 kPa and 293.2 K; effect of temperature (293.2–313.2 K) on the SO_2 absorption isotherms for (b) $[N_{2222}][HSO_4]$, (c) $[N_{4444}][HSO_4]$, (d) $[N_{6666}][HSO_4]$ at 100 kPa; (e) polarizing microscope images of $[N_{2222}][HSO_4]$ and $[N_{4444}][HSO_4]$ before and after absorption of SO_2 (scale bars: 200/500 μm).

using Gaussian 16 program at B3LYP/6-311 + G(2d,p) level, with D3 (BJ) dispersion correction to account for deviations in the description of weak interactions. Subsequently, single-point energy calculations were carried out on the optimized structures using the def2-TZVP basis set to obtain more accurate energy information, and corresponding *.COSMO files were generated for COSMOtherm 2021 software to calculate the σ–profiles and σ–potentials of the AQA-HSO_4 ILs and SO_2.(Weigend and Ahlrichs 2005; Weigend 2006; Zhao and Truhlar 2007) Based on the optimized geometries, ESP (electrostatic potential) and IGMH (independent gradient model based on Hirshfeld partitioning) analysis were performed using Multiwfn 3.8 Dev.(Lu and Chen 2012; Zhang and Lu 2021; Lu and Chen 2022) The resulting data were visualized with VMD (Visual Molecular Dynamics), wherein high-resolution spatial grids were constructed to generate color-filled isosurfaces that intuitively reveal the spatial distribution of weak interactions between AQA-HSO_4 ILs and SO_2.

3. Results and discussion

The molecular structures of AQA-HSO_4 ILs were confirmed by ^1H and ^{13}C NMR and the detailed spectral data are provided in the Supporting Information (see Fig. S2-S7). The effects of alkyl chain length on the melting point (M.P.) and thermal stability of AQA-HSO_4 ILs were evaluated, and the corresponding results are shown in Fig. S8 and Table 1. The results show that AQA-HSO_4 ILs have good thermal stability, with decomposition temperatures (T_d) above 475.2 K, which confirms that these ILs can remain structurally stable under typical conditions of SO_2 separation. In addition, it can be found that the M.P and T_d values of AQA-HSO_4 ILs are inversely correlated with the alkyl chain length (C2, C4 and C6). These trends can be attributed to the electron-donating and steric effects of longer alkyl chains weaken the Coulombic interactions and reduce charge density between the cations and $[HSO_4]^-$ anion. It is well known that SO_2 is commonly captured by ILs through absorption sites or physical dissolution, and subsequently stabilized between cations and anions within their electrostatic field. Given that AQA-HSO_4 ILs

Table 1
Physical properties and SO_2 absorption performance of AQA-HSO_4 ILs at 100 kPa and 293.2 K.

AQA-HSO_4 ILs	M_W[a] (g mol^{-1})	T_d[b] (K)	M.P.[c] (K)	SO_2 uptake (mmol g^{-1})	S_{50}[d] (mmol g^{-1} min^{-1})	IAST[e] (SO_2/CO_2)
$[N_{2222}][HSO_4]$	227.3	574.2	475.2	3.0	2.29	682
$[N_{4444}][HSO_4]$	338.5	548.2	430.2	7.1	1.33	855
$[N_{6666}][HSO_4]$	451.8	475.2	336.2	5.7	2.18	518

[a] The molecular weight; [b]decomposition temperature; [c]melting point; [d]half-saturation absorption factor; [e]IAST selectivity (SO_2/CO_2, v/v = 50:50).

studied here are solid at room temperature and contain the $[HSO_4]^-$ anion. It is reasonable to assume that SO_2 may interact with the acidic hydrogen of $[HSO_4]^-$ via hydrogen bonds and become stabilized within the ion pair. Therefore, it is essential to determine whether the physical state of AQA-HSO_4 ILs with different alkyl chains changes upon SO_2 absorption, and how such phase behavior affects the overall absorption capacity as well as the associated thermodynamic and kinetic processes.

3.1. SO_2 absorption

The SO_2 absorption performance and phase transition behaviors of AQA-HSO_4 ILs were investigated at 100 kPa and 293.2–313.2 K, as shown in Fig. 1a. The results show that the extension of the cationic alkyl chain from ethyl to butyl and hexyl causes the SO_2 absorption isotherms of AQA-HSO_4 ILs to evolve from a nonlinear isotherm, gradually increasing profile into a nearly linear exhibiting pronounced inflection points at specific partial pressures. This trend suggests that SO_2-triggered phase transition of AQA-HSO_4 ILs is a pressure-dependent process characterized by specific partial pressure thresholds. As shown in Fig. 1a, the threshold values are highly sensitive to the cationic alkyl chain length. For the longest-chain $[N_{6666}][HSO_4]$, phase transition occurs at negligible SO_2 partial pressures (~1 kPa), indicating a highly unstable solid lattice that is easily disrupted by SO_2 molecules. Conversely, $[N_{4444}][HSO_4]$ exhibits a clear threshold at ~50 kPa and 293.2 K, where SO_2 uptake capacity rises abruptly from 0.67 mmol g^{-1} to 7.1 mmol g^{-1} after liquefaction. The shorter-chain $[N_{2222}][HSO_4]$ remains entirely solid within 0–100 kPa, with no detectable phase transition. This correlation suggests that increasing the alkyl chain length effectively lowers the energy barrier for the solid-to-liquid transition by shielding the ionic charges and weakening the inter-ionic Coulombic forces. In addition, absorption temperature further exerts a pronounced regulatory effect on the self-phase-transition behavior of AQA-HSO_4 ILs (see Fig. 1b-1d). For example, when the SO_2 absorption temperature of $[N_{4444}][HSO_4]$ increases from 293.2 K to 313.2 K, the onset SO_2 partial pressure required to trigger the self-phase-transition rises from 49.5 kPa to 93.4 kPa (Fig. 1c, purple circle). In contrast, $[N_{6666}][HSO_4]$ still undergoes a rapid solid to liquid phase-transition at low SO_2 partial pressures, while $[N_{2222}][HSO_4]$ remains entirely solid throughout the whole pressure range under the test conditions, with its SO_2 uptake inflection point locked at ~60 kPa (see Fig. 1d). Besides, Fig. 1e presents the polarizing microscopy images of $[N_{2222}][HSO_4]$ and $[N_{4444}][HSO_4]$ before and after SO_2 absorption, which were used to assess their micromorphological changes. The results show that $[N_{2222}][HSO_4]$ remained in its solid state throughout the absorption process, with no discernible change in morphology. In contrast, $[N_{4444}][HSO_4]$ exhibited a distinct phase transition, completely converting into a liquid phase upon SO_2 uptake. Overall, these results indicate that longer cationic alkyl chains weaken ionic interactions and facilitate the insertion of SO_2 into the ion pair. Furthermore, the results also suggest that SO_2-triggered self-phase transition enables a dual-mode operational scheme for AQA-HSO_4 ILs, allowing stable solid-state storage under idle conditions and fluidic liquid-phase behavior during active operations to enhance both absorption and separation efficiency. Subsequently, the effects of absorption temperatures on the SO_2 uptake capacity of AQA-HSO_4 ILs were evaluated. As shown in Fig. 1b-1c, the SO_2 absorption capacity of the three ILs decreases with increasing temperature, which is consistent with the thermodynamic law that gas solubility decreases with increasing temperature. Therefore, the results also suggest that moderately tuned alkyl groups may promote more sensitive phase transition responses, which means that AQA-HSO_4 ILs have the potential to separate higher purity SO_2 from mixed gas.

In separation and purification engineering, although the capacity of an absorbent is a key parameter, its absorption rate and mass transfer efficiency are even more critical in determining the feasibility and economic viability of its industrial application. Fig. 2a shows the kinetic curves of SO_2 absorption by AQA-HSO_4 ILs at 293.2 K and 100 kPa. It was observed that all AQA-HSO_4 ILs exhibited rapid SO_2 absorption rates in the initial stage. Specifically, the SO_2 absorption capacities of AQA-HSO_4 ILs increased sharply within 0–5 min, after which the absorption rates gradually decelerated until SO_2-saturation was reached (~30 min). The final SO_2 uptake capacities were consistent with SO_2 absorption isotherm results. It is worth noting that $[N_{4444}][HSO_4]$ absorbed 67% of the total SO_2 absorption capacity within 5 min, which means that it has the potential to efficiently separate SO_2. In addition, $[N_{4444}][HSO_4]$ exhibits a unique rate transition within the first 0.5 min, which is closely related to its spontaneous SO_2-triggered solid-to-liquid phase transition (see Fig. 2a, inset). During the initial stage, SO_2 absorption rate of $[N_{4444}][HSO_4]$ is slightly lower than that of $[N_{6666}][HSO_4]$, as the latter liquefies almost instantaneously upon exposure SO_2. However, as SO_2 continuously dissolves, the absorption rate of $[N_{4444}][HSO_4]$ soared dramatically with the onset of the solid–liquid phase transition. The results support that the essence of solid-to-liquid phase transition effectively surmounts the limitations of slow solid-phase diffusion, facilitating a shift toward rapid and efficient gas–liquid diffusion. The formation of the liquid phase lowers the energy barrier for SO_2 molecules to migrate into the bulk of $[N_{4444}][HSO_4]$ system. This process allows the $[HSO_4]^-$ active sites buried within the interior to become fully exposed and utilized, which leads to a steeper slope of the absorption capacity curve. As a result, this phase transition-induced amplification effect of SO_2 absorption rate compensates for the initial mass transfer limitations associated with its medium-length alkyl chains, enabling $[N_{4444}][HSO_4]$ to achieve an optimal balance between absorption rate and capacity. On the other hand, $[N_{2222}][HSO_4]$ remains solid throughout the entire process, which markedly limits its SO_2 absorption rate and final capacity.

Moreover, the SO_2 absorption rate data were fitted using pseudo-first-order (PFO) and pseudo-second-order (PSO) kinetic models, and the results are shown in Fig. 2b.(Khamizov 2020; Guo and Wang 2019) For all three ILs, PSO model yields higher correlation coefficients ($R^2 >$ 0.978) compared to PFO model, which indicates that the SO_2 absorption process is better described by PSO kinetics. The result implies that the absorption rate is not solely governed by physical diffusion but is also strongly influenced by hydrogen bonds and electrostatic interactions between SO_2 and the constituent ion pairs. As expected, the solid-state $[N_{2222}][HSO_4]$ exhibits the highest k_2 value (0.301 min^{-1}) yet the lowest total SO_2 absorption capacity (3 mmol g^{-1}) highlights the difference between site accessibility and macroscopic performance. Therefore, SO_2 absorption of $[N_{2222}][HSO_4]$ is limited by poor site accessibility due to solid-phase diffusion, resulting in a low effective capacity. In contrast, although $[N_{4444}][HSO_4]$ and $[N_{6666}][HSO_4]$ exhibit relatively lower k_2 values (0.121 and 0.155 min^{-1}), they achieve higher SO_2 absorption efficiency due to the advantages of phase transition. Meanwhile, the Weber-Morris intraparticle diffusion model was employed to decouple the complex mass transfer steps, and the analysis is conducted by plotting SO_2 absorption capacity against the square root of time ($t^{0.5}$).(Pan et al. 2024; Wang et al. 2024) As depicted in Fig. 2c,

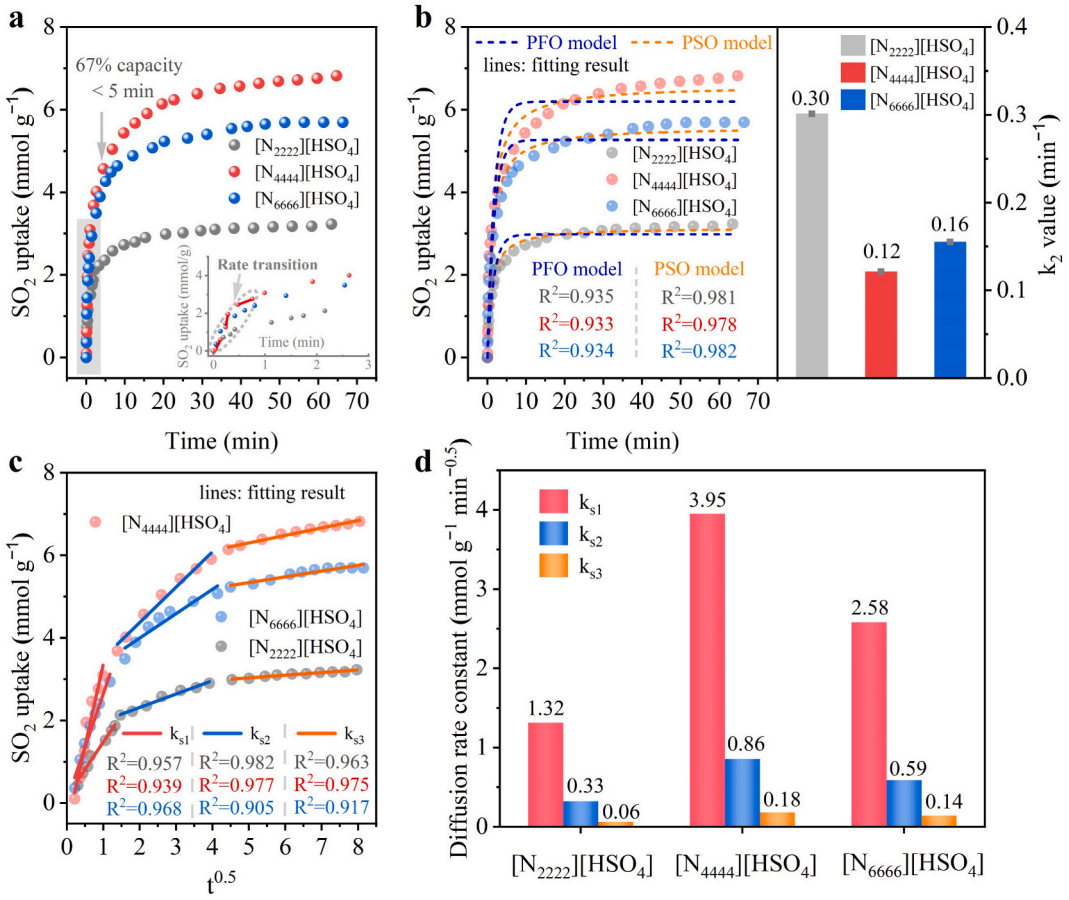

Fig. 2. (a) The SO_2 absorption rate curves of AQA-HSO_4 ILs at 100 kPa and 293.2 K; (b) SO_2 absorption kinetics curves fitted using PFP and PSO models at 100 kPa and 293.2 K, including rate constants (k_2) and correlation coefficients (R^2); (c) Weber-Morris intraparticle diffusion plots of SO_2 uptake against $t^{0.5}$, and (d) the corresponding diffusion rate constants for the three stages (k_{s1}, k_{s2}, k_{s3}).

SO_2 absorption curves of AQA-HSO_4 ILs were divided into three stages ($R^2 > 0.9$), which signifies that total SO_2 absorption is a complex process co-controlled by several steps, not solely by free molecule diffusion. It can be surmised that these three steps can be regarded as an initial external film diffusion stage (k_{s1}), a subsequent intra-IL diffusion stage (k_{s2}), and a final equilibrium stage (k_{s3}), and the corresponding results are shown in Fig. 2d. The kinetic analysis confirms that AQA-HSO_4 ILs followed the general trend of $k_{s1} > k_{s2} > k_{s3}$, implying that the overall absorption efficiency is primarily governed by the combination of external film diffusion and intra-IL diffusion. In addition, $[N_{4444}][HSO_4]$ exhibited superior rate constants ($k_{s1\text{-}s3}$) across all three stages compared to its counterparts, which corroborates that the phase transition, facilitated by the fine tuning of the alkyl chain length, effectively and simultaneously surmounts the mass transfer barriers inherent to both external and internal diffusion processes.

Furthermore, SO_2 absorption isotherms show that the phase transitions for $[N_{4444}][HSO_4]$ and $[N_{6666}][HSO_4]$ corresponded to SO_2 uptakes of 0.67 and 0.59 mmol g^{-1}, respectively (see Fig. 1a). The absorption times from the SO_2 absorption rate curves were 0.134 and 0.108 min, which may be interpreted as an instantaneous solid-to-liquid transition. Furthermore, we considered that $[N_{2222}][HSO_4]$ remains in a solid state throughout the SO_2 absorption process. The two-film theory to estimate the liquid-side volumetric mass transfer coefficients (k_La) for $[N_{4444}][HSO_4]$ and $[N_{6666}][HSO_4]$ systems at 293.2 K and 100 kPa (see Fig. S9).(Iliuta, Hasib-ur-Rahman, and Larachi 2014; Ortiz et al. 2010) The results show that the k_La for $[N_{4444}][HSO_4]$ is 3.08×10^3 s^{-1}, while the value for$[N_{6666}][HSO_4]$ is 4.31×10^3 s^{-1}; these are greater than the previously reported value (2.41×10^3 s^{-1}) for the [Py][DiEtSO$_4$] with SO_2 system.(Hui et al. 2025) These findings suggest that $[N_{4444}][HSO_4]$ exhibits excellent mass transfer properties for SO_2 absorption and possesses significant potential for engineering applications. Besides, the gas absorption and separation processes are usually operated under non-saturated conditions, often reaching >50% of the saturation capacity to enhance the operational efficiency of the absorption tower. Therefore, the working efficiency of AQA-HSO_4 ILs was evaluated using the half-saturation absorption factor (S_{50}), defined as the time required to reach 50% of the total SO_2 absorption capacity, as shown in Table 1. (Chen et al. 2022) The results indicate that $[N_{4444}][HSO_4]$ has an acceptable value of 1.33mmol g^{-1} min^{-1}. This allows the absorbent to efficiently capture half SO_2 capacity (3.55 mmol g^{-1}) within 2.66 min. Notably, this partial uptake achieved in less than three minutes already surpasses the total SO_2 capacity (3 mmol g^{-1}) of $[N_{2222}][HSO_4]$ reached after 30 min. As established by the full kinetic profile (Fig. 2a), the phase transition in $[N_{4444}][HSO_4]$ ensures its total SO_2 absorption efficiency is outstanding, which means that $[N_{4444}][HSO_4]$ is a potential candidate for efficient SO_2 capture.

3.2. SO_2 absorption mechanism

The absorption mechanism of SO_2 by AQA-HSO_4 ILs at different times were analyzed using in-situ FT-IR. Initially, conventional FT-IR spectra of fresh AQA-HSO_4 ILs (solid state) were recorded for spectral comparison, with KBr as background. Subsequently, SO_2 absorption process of AQA-HSO_4 ILs was monitored in real-time using in-situ FT-IR. As shown in Fig. 3, it can be observed that fresh and SO_2-absorbed AQA-HSO_4 ILs exhibit characteristic absorption bands assigned to the alkyl chains of the cation. Stretching vibrations for the methyl ($-CH_3$) groups are observed at 2962c m^{-1} and 2876 cm^{-1}, whereas the methylene

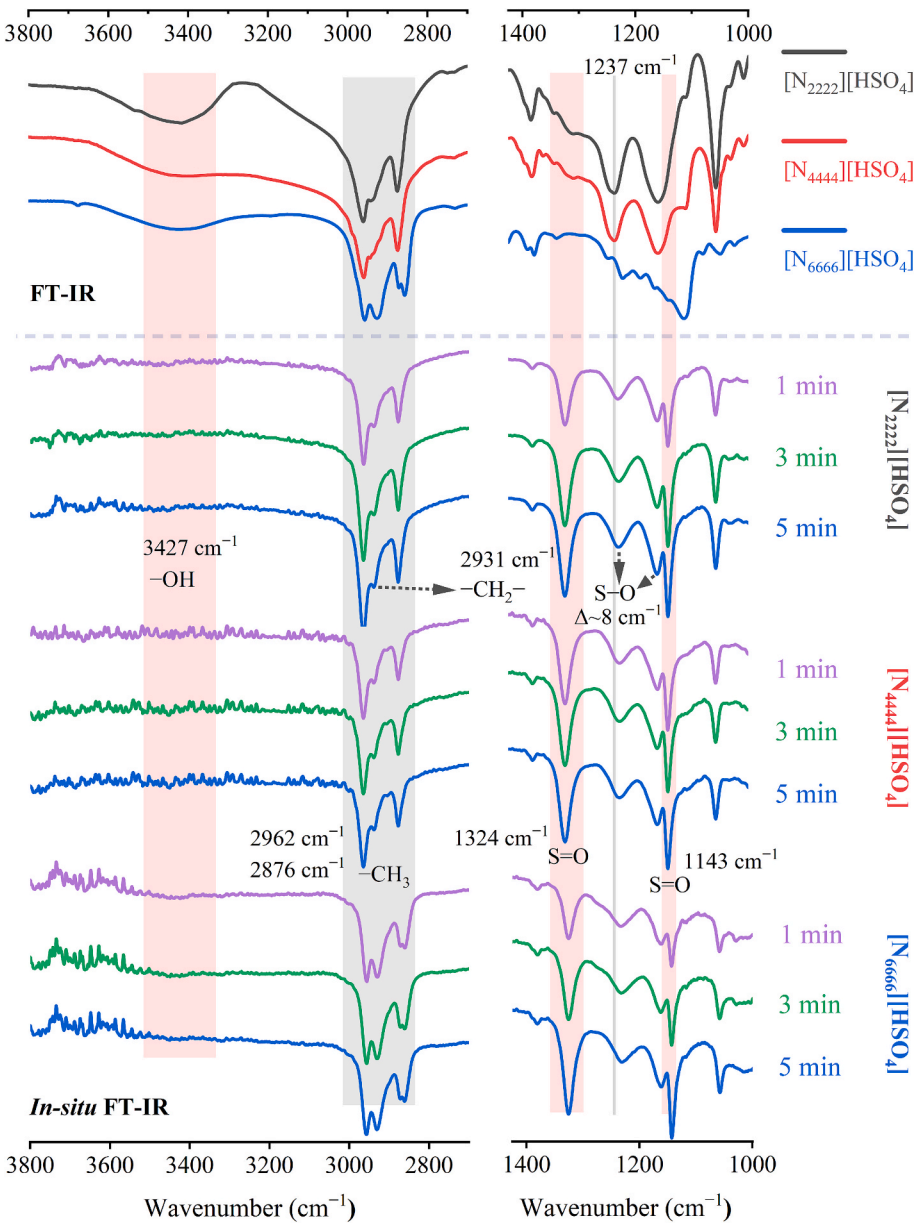

Fig. 3. Conventional FT-IR and in-situ FT-IR spectra of SO_2 uptake at different times (1, 3, 5 min) using AQA-HSO_4 ILs as absorbent at 293.2 K at atmospheric pressure, with SO_2 flow rate is 40 mL min^{-1}.

(–CH_2–) group vibration is located at 2931 cm^{-1} (left side, Fig. 3).(Deng, Liu, and Gao 2017) Moreover, progressive increase in the peak intensity of –CH_2– band is noted, which corresponds to the elongation of the alkyl chains. Notably, –OH vibration band at 3427 cm^{-1} completely disappears after SO_2 absorption in AQA-HSO_4 ILs, accompanied by the appearance of distinct new peaks at 1324 cm^{-1} and 1143 cm^{-1} (right side, Fig. 3).(Sun et al. 2015; Jiang et al. 2019) These newly formed bands are attributed to the asymmetric and symmetric S=O stretching vibrations of the absorbed SO_2, which are notably shifted from the vibrational frequencies of free SO_2 (1360 cm^{-1} and 1050 cm^{-1}).(Lee et al. 2016; Wang et al. 2017) The simultaneous disappearance of –OH and emergence of SO_2 peaks provide definitive evidence for the formation of a strong hydrogen bond between $[HSO_4]^-$ anion and SO_2 molecule. Meanwhile, this result is further substantiated by redshift (Δ ~8 cm^{-1}) of S-O stretching vibration from 1237 cm^{-1} in SO_2-absorbed AQA-HSO_4 ILs, which indicates an alteration of its electronic environment due to the interaction.(Wang et al. 2017) Therefore, these results support that $[HSO_4]^-$ anion serves as the primary active site for SO_2 capture.

3.3. SO_2 selective absorption

The practical viability of SO_2 absorbents hinges on their ability to selectively capture SO_2 from complex gas mixtures, such as competing CO_2 or N_2. The absorption isotherms for SO_2, CO_2 and N_2 at 293.2 K and 100 kPa were measured to evaluate SO_2 selective separation performance of AQA-HSO_4 ILs (see Fig. 4a and Fig. S10). The results reveal that $[N_{4444}][HSO_4]$ has an exceptional affinity and capacity for SO_2, contrasted with a virtually non-existent CO_2 uptake. This difference is attributed to the distinct phase behaviors of AQA-HSO_4 ILs upon interaction with SO_2 or CO_2. In other words, AQA-HSO_4 ILs are inert to CO_2 and do not undergo a phase transition, thus preventing significant CO_2 uptake. For example, $[N_{4444}][HSO_4]$ absorbed 7.1 mmol g^{-1} of SO_2 while CO_2 uptake was a mere 0.0083 mmol g^{-1}. Based on the Ideal Adsorbed Solution Theory (IAST), SO_2/CO_2 selectivity for $[N_{4444}][HSO_4]$ was calculated to be 855, which means that this IL can efficiently

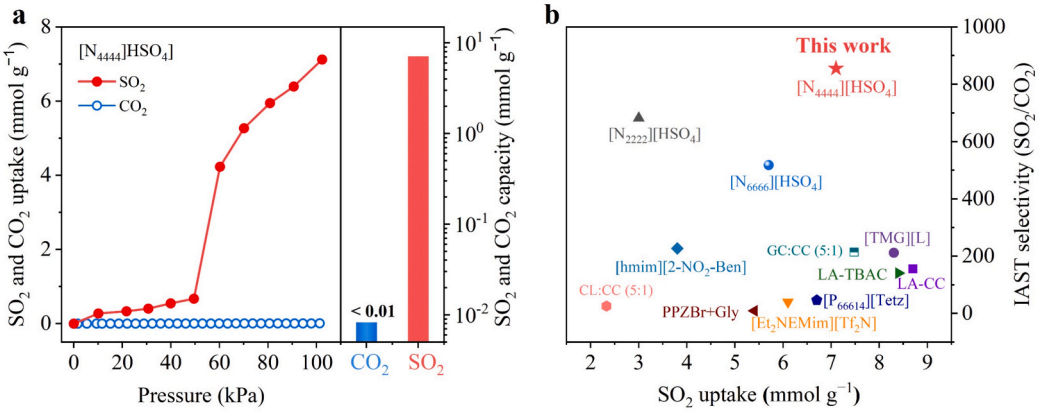

Fig. 4. (a) Selective absorption isotherms and capacities for SO_2 and CO_2 using $[N_{4444}][HSO_4]$ at 293.2 K and 100 kPa; (b) comparison of SO_2/CO_2 IAST selectivities between AQA-HSO_4 ILs and other reported ILs absorbents.

separate SO_2 with a purity greater than 99.99% from SO_2/CO_2 mixtures. Furthermore, this trend of high selectivity remained consistent across the homologous series, both $[N_{2222}][HSO_4]$ and $[N_{6666}][HSO_4]$ also demonstrated negligible CO_2 uptake, measured at 0.0044 mmol g^{-1} and 0.011 mmol g^{-1}, respectively. Consequently, $[N_{2222}][HSO_4]$ and $[N_{6666}][HSO_4]$ ILs achieved remarkably high SO_2/CO_2 IAST selectivities of 682 and 518 (see Fig. S10). As shown in the comparative analysis in Fig. 4b, $[N_{4444}][HSO_4]$ significantly outperforms previously reported IL systems in terms of SO_2/CO_2 selectivity.(Huang, Wu, and Hu 2016; Liu, Gao, and Deng 2018; Cui et al. 2019; Wang et al. 2011; Yang et al. 2013; Wu et al. 2004; Deng, Han, and Jiang 2015) Additionally, Fig. S11 shows AQA-HSO_4 ILs also exhibit negligible N_2 uptake, SO_2 capacities ranging from only 0.013 mmol g^{-1} to 0.088 mmol g^{-1} at the same conditions. Combined with practically non-existent CO_2 affinity of $[N_{4444}][HSO_4]$, these results demonstrate that SO_2 capture process is highly selective even in the presence of common competing gases. Therefore, these findings suggest that the pronounced preference for SO_2 over CO_2 and N_2 demonstrates the ability of $[N_{4444}][HSO_4]$ to efficiently and selectively capture SO_2 from complex gas mixtures, positioning it as a highly promising absorbent for industrial emission control and sulfur resource recovery.

3.4. DFT and COSMOtherm analysis

To investigate the sites for intermolecular non-covalent interaction, the optimized geometries of AQA-HSO_4 ILs, SO_2 and CO_2 were obtained via DFT calculations, and their surface electrostatic potential (ESP) distributions were analyzed.(Zhang and Lu 2021; Lu and Chen 2012) As shown in Fig. 5a-5c, the negative potential (−49.37 ~ −61.71 kcal mol^{-1}) of the three ILs is highly concentrated on O atoms of the $[HSO_4]^-$ anion, which indicates that the $[HSO_4]^-$ anion serves as the primary active site for interaction with acidic gas molecules. Conversely, the positive potential (+29.61 ~ +38.02 kcal mol^{-1}) is predominantly distributed on the central N atom of the quaternary ammonium cation and its adjacent methylene H atoms. It is worth noting that as the alkyl chain is elongated from ethyl (N_{2222}) to hexyl (N_{6666}), the more diffuse positive potential on the cation due to the shielding effect, and the concomitant sharp increase in the proportion of the weak polar surface area. This structural change is expected to weaken the Coulombic interactions between the ion pairs and potentially increase susceptibility to phase transition, which is in line with the phase transition phenomenon observed in SO_2 absorption tests. In addition, distinct positive potential regions (i.e., +34.00, +25.88 and +29.26 kcal mol^{-1}) are observed around the acidic H atom of the $[HSO_4]^-$ anion, which serves as an electrophilic site capable of attracting electron-rich species. For SO_2 and CO_2 molecules (Fig. 5d and Fig. 5e), SO_2 exhibits strong polarity in contrast to nonpolar CO_2, with its S atom possesses a strong positive potential (+34.00 kcal mol^{-1}), while its O atoms are negative potential (−19.96 kcal mol^{-1}). Therefore, the results suggest that the interaction between SO_2 and the $[HSO_4]^-$ anion is expected to be stronger than that with CO_2.

Subsequently, the COSMOtherm was employed to evaluate the interaction probability and dissolution capacity of AQA-HSO_4 ILs with SO_2/CO_2 by analyzing the surface charge distribution (σ-profile) and

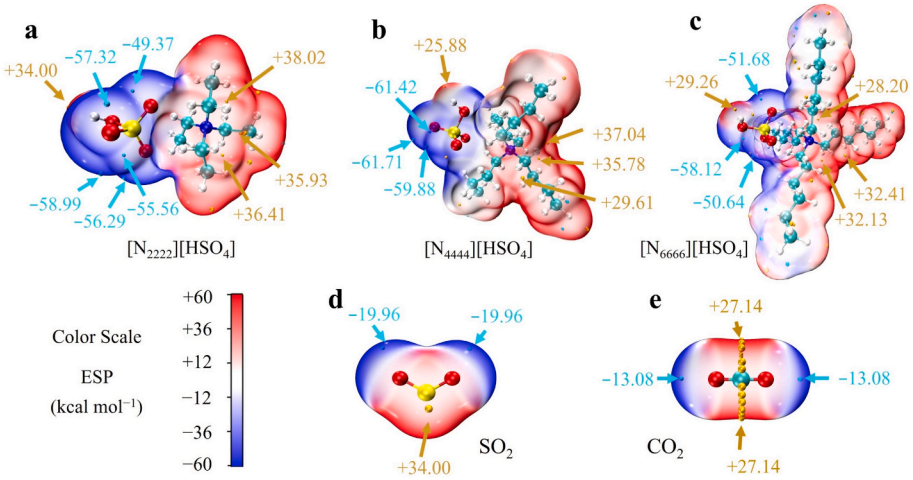

Fig. 5. Optimized molecular geometries and surface electrostatic potential maps of AQA-HSO_4 ILs, SO_2 and CO_2 calculated at the B3LYP/6–311 + G(2d,p) level.

surface chemical potential (σ-potential) of each species (see Fig. 6).(Lu and Chen 2012; Zhang and Lu 2021) Based on the features of the σ values, the σ-profile is demarcated into three regions using ± 0.0084 e $Å^{-2}$ as thresholds: the hydrogen-bond donor (HBD) region, the nonpolar region, and the hydrogen-bond acceptor (HBA) region (see Fig. 6b). Firstly, AQA-HSO_4 ILs exhibit distinct peaks in both the nonpolar and HBA regions, which are attributed to the contributions of the alkyl chains and the $[HSO_4]^-$ anion, respectively. The results demonstrate that the intensity and area of the nonpolar peaks follow the trend of increasing nonpolar surface area observed in the ESP analysis $[N_{6666}][HSO_4] > [N_{4444}][HSO_4] > [N_{2222}][HSO_4]$. Concurrently, the order of peak intensities and areas for the three ILs in the HBA region is inverted relative to that in the nonpolar region (inset, Fig. 6b). It can be inferred that the increasing length of the alkyl chain diminishes the apparent HBA capability of the $[HSO_4]^-$ anion due to steric hindrance or shielding effects. The σ-profile of SO_2 shows distribution at both ends of ± 0.0084 e $Å^{-2}$, indicating a strong amphiphilic character, whereas the polar region distribution for CO_2 is relatively weaker. Additionally, the similarity in the σ-profile of SO_2 within the negatively charged region to that of AQA-HSO_4 ILs supports that the long-chain AQA-HSO_4 ILs are particularly susceptible to phase transitions after SO_2 uptake.

Furthermore, the σ-potential (μ(σ), Fig. 6c) reveals the chemical potential of a molecular segment with a specific surface charge density σ in the corresponding pure absorbent, and the lower μ(σ) value implies that the interactions are more favorable. Comparing the μ(σ) curves of the species, it is found that SO_2 (+0.32 kcal mol^{-1} $Å^{-2}$) has a lower positive chemical potential in the HBD and HBA region than CO_2 (+0.46 kcal mol^{-1} $Å^{-2}$). In addition, it is observed that $[N_{4444}][HSO_4]$ has a more negative μ(σ) in the HBD region together with an elevated μ(σ) in the HBA region, which is a favorable balance of hydrogen-bond interactions that provides evidence for its optimal SO_2 absorption performance (inset, Fig. 6c). Besides, the polar fragments on the surface of the SO_2 molecule ($S\delta^+$ and $O\delta^-$) have a suitable interaction affinity with the polar environment provided of $[HSO_4]^-$anion. This electronic complementarity facilitates a multipoint interaction mode, which promotes the preferential stabilization of SO_2 within the ion pair. As a result, these findings indicate that the polar environments of AQA-HSO_4 ILs provide favorable conditions for hydrogen-bonding interaction and Coulombic interaction with SO_2. Meanwhile, it is noteworthy that the chemical potential of AQA-HSO_4 ILs becomes progressively more favorable with increasing alkyl chain length and corresponds to the μ(σ) potential of SO_2 in that region, which suggests a stronger affinity for SO_2 than for CO_2. Additionally, the chemical potential distributions of SO_2 and AQA-HSO_4 ILs are concentrated in the nonpolar region, indicating that SO_2 absorption in these ILs is governed predominantly by physical rather than chemical interactions.

The host–guest interaction properties and strengths between AQA-HSO_4 ILs and SO_2/CO_2 were analyzed by DFT, and their inter- and intra-fragment interactions via isosurface analysis (see Fig. 7 and Fig. 8). IGMH analysis reveals a clear difference between the interactions of AQA-HSO_4 ILs with SO_2 and CO_2.(Lu and Chen 2022) In AQA-HSO_4 ILs-SO_2 system (Fig. 7a-7c), large blue green isosurfaces were observed between the $[HSO_4]^-$ anion and the SO_2, corresponding to hydrogen bonds and Coulombic interactions, which corroborate the predictions from ESP and COSMO analyses. In particular, the isosurfaces indicate that hydrogen bond occurs between the acidic proton and SO_2, while the Coulombic attraction between the electrophilic $S\delta^+$ of SO_2 and the $O\delta^-$of $[HSO_4]^-$ acts as a secondary force that strengthens the overall interaction. On the other hand, the interactions between CO_2 and AQA-HSO_4 ILs were weak, with uniformly bright green isosurfaces confirming that CO_2 is constrained only by weak non-directional Van der Waals forces and lacks the strong directional interactions observed for SO_2 (Fig. 7d-7f). These findings further demonstrate that the ultrahigh SO_2/CO_2 IAST selectivity (up to 855) of AQA-HSO_4 ILs arises from the fundamental difference in interaction modes. Moreover, the green isosurfaces became more extensive and denser as the cationic alkyl chain length increased from ethyl ($[N_{2222}]^+$) to hexyl ($[N_{6666}]^+$), which indicates an enhanced contribution of Van der Waals interaction. This result is consistent with the slight increase in CO_2 uptake observed for $[N_{2222}][HSO_4]$ (0.0044 mmol g^{-1}), $[N_{4444}][HSO_4]$ (0.0083 mmol g^{-1}), and $[N_{6666}][HSO_4]$ (0.011 mmol g^{-1}). Therefore, the modulation of alkyl chain length not only effectively regulates phase-transition behavior but also provides a viable strategy for tuning SO_2 separation performance.

The key atomic distances and interaction energies (ΔE) between AQA-HSO_4 ILs and SO_2/CO_2 were assessed by DFT analysis based on optimized structures (see Fig. 8). The results show that AQA-HSO_4 ILs interact with SO_2 and CO_2 through hydrogen bonds and Coulombic forces involving the anion and form hexagon-like stable structures. Meanwhile, the calculated ΔE values of AQA-HSO_4 ILs with SO_2 or CO_2 were below the threshold of 40 kJ mol^{-1} for chemical absorption, suggesting that both processes are physical absorption, in line with SO_2/

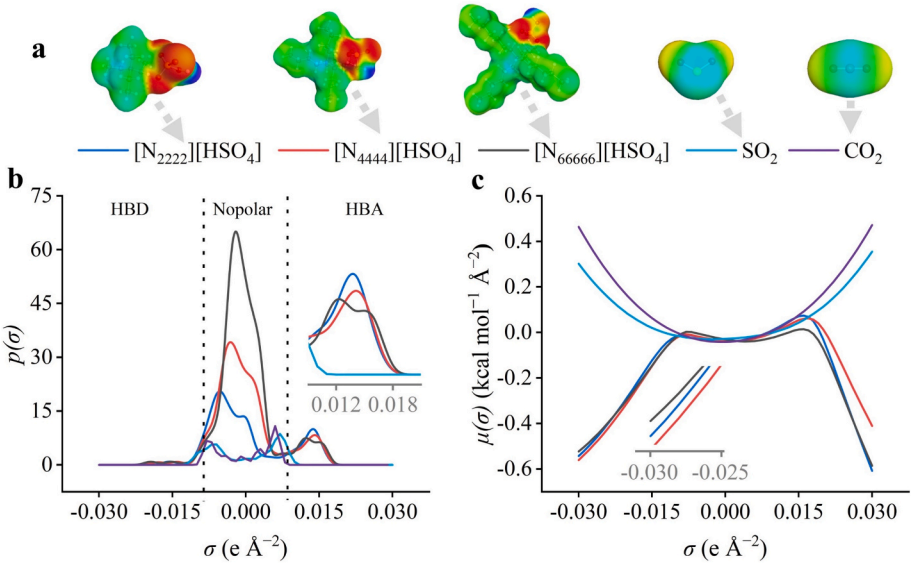

Fig. 6. (a) Surface charge density distribution, (b) σ-profile p(σ), and (c) chemical potential μ(σ) analysis for AQA-HSO_4 ILs, SO_2 and CO_2 calculated via COSMOtherm.

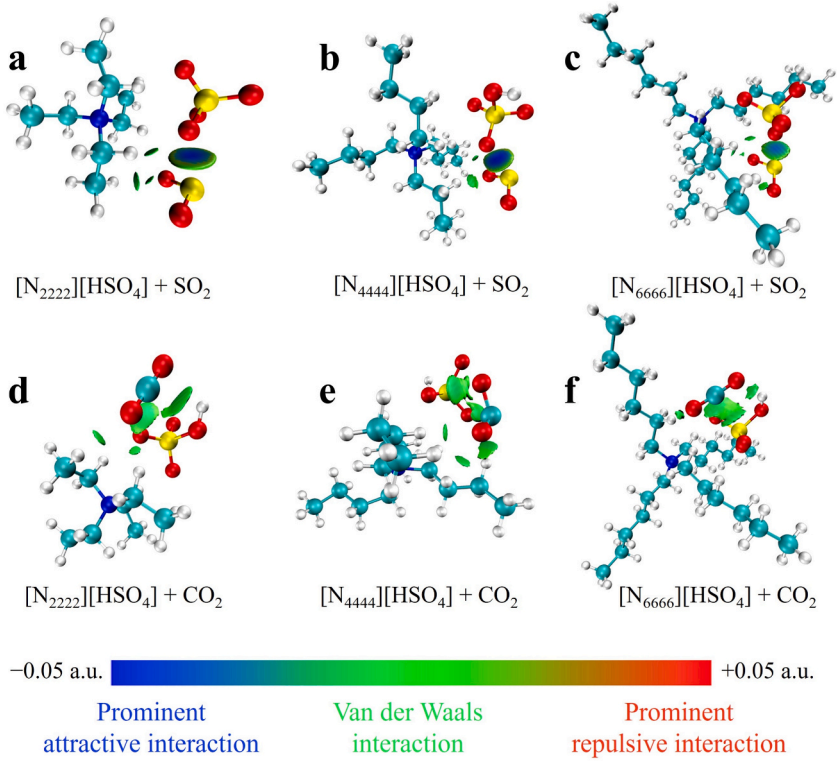

Fig. 7. IGMH analysis of inter- and intra-fragment weak interactions between AQA-HSO_4 ILs and SO_2/CO_2, and isovalue = 0.01 a.u., surface sign range = −0.05 to 0.05 a.u.

CO_2 absorption behavior tested in the absorption experiment. In short, ΔE values of AQA-HSO_4 with SO_2 range from −19.32 to −33.24 kJ mol^{-1}, which is slightly higher than the typical physical absorption range (<20 kJ mol^{-1}), and is indicative of stronger interactions (Fig. 8a-8c). In contrast, AQA-HSO_4 ILs-CO_2 system exhibits weaker interaction (<−10.11 kJ mol^{-1}), characteristic of typical physical absorption (Fig. 8d-8f). Furthermore, ΔE values for both SO_2 and CO_2 increased with the elongation of the cationic alkyl chain, suggesting that the enhanced Van der Waals forces compensate for potential shielding and steric hindrance effects, thereby stabilizing the overall binding of both gas molecules. Notably, the distance between the S atom of SO_2 and O atom of HSO_4^- was extremely short in AQA-HSO_4 ILs-SO_2 system. For example, in [N_{4444}][HSO_4]-SO_2 system, the H and O atom distance was only 1.83 Å, which provides clear evidence for formation of hydrogen bonds (Fig. 8b). The S and O atom distance (2.37 Å) further confirmed the presence of a multipoint cooperative binding mode. By comparison, the atomic distances between H···O (2.19–2.28 Å) and C···O (2.59–2.79 Å) in AQA-HSO_4 ILs-CO_2 system were significantly longer, indicating much weaker interactions (Fig. 8d-8f). Moreover, in the [N_{4444}][HSO_4] system, ΔE value with SO_2 was more than −20 kJ mol^{-1} lower than that with CO_2 (−9.07 kJ mol^{-1}). This ΔE value difference ensures that [N_{4444}][HSO_4] overwhelmingly favors SO_2 capture under competitive absorption conditions. Meanwhile, molecular dynamics (MD) simulations were performed for the [N_{4444}][HSO_4] systems absorbing SO_2 and CO_2, and the corresponding radial distribution functions (RDFs) were calculated. As shown in Fig. 8g, [N_{4444}][HSO_4]-SO_2 system exhibits a sharper and more intense first peak, whereas [N_{4444}][HSO_4]–CO_2 system shows the opposite trend. Moreover, the peak position for the [N_{4444}][HSO_4]-SO_2 system appears at 2.77 Å, while that for CO_2 shifts to 3.04 Å. The results indicate that the interaction between SO_2 and the anion in [N_{4444}][HSO_4] is stronger than that of CO_2, implying that the enhanced affinity promotes the preferential absorption of SO_2 by [N_{4444}][HSO_4]. Therefore, these findings provide strong evidence for the high SO_2/CO_2 selectivity of AQA-HSO_4 ILs, supporting their potential as a candidate for selective SO_2 separation.

3.5. Recycle test

The reusability and long-term operational stability of absorbents are as crucial as their uptake capacity and selectivity for practical engineering applications. Consequently, the performance of the optimal [N_{4444}][HSO_4] was evaluated through extended SO_2 absorption–desorption cycles at 293.2 K and 100 kPa. As shown in Fig. 9a, [N_{4444}][HSO_4] maintained a satisfactory SO_2 absorption capacity (~7.1 mmol g^{-1}) over 20 consecutive cycles, without any observable SO_2 capacity loss. Notably, the regeneration proceeded without heating, and nearly complete SO_2 desorption was achieved simply by depressurizing to ~20 kPa for 2 h or vacuum for 0.5 h at the absorption temperature (see Fig. S12). These results indicate that [N_{4444}][HSO_4] has excellent cycle stability and facile regenerability. Moreover, the reversible phase transition behavior of [N_{4444}][HSO_4] was visually documented to provide intuitive evidence of its macro-physical evolution. As shown in Fig. 9b, the absorbent undergoes a distinct transformation from a white solid to a transparent yellow liquid upon SO_2 absorption, and fully reverts to its original solid state after regeneration. In addition, FT-IR spectral (see Fig. 9c) comparisons between fresh samples and those regenerated after cycles revealed that the two spectra had near-identical profiles, which confirms that [N_{4444}][HSO_4] retains structural integrity even after repeated SO_2 uptake and release processes. To further demonstrate the rapid phase transition characteristics of [N_{4444}][HSO_4] during SO_2 absorption and desorption, the evolution of its state of matter was recorded using a transparent integrated absorber (see Video.mp4 in Appendix B). Additionally, a series of representative time-lapse snapshots extracted from the experimental video are presented in Fig. 9d. It can be observed that the solid [N_{4444}][HSO_4] undergoes an almost instantaneous solid-to-liquid transition upon contact with SO_2, indicating a rapid and sensitive response to SO_2 gas. Correspondingly, the liquid phase swiftly recrystallizes into a solid powder during vacuum

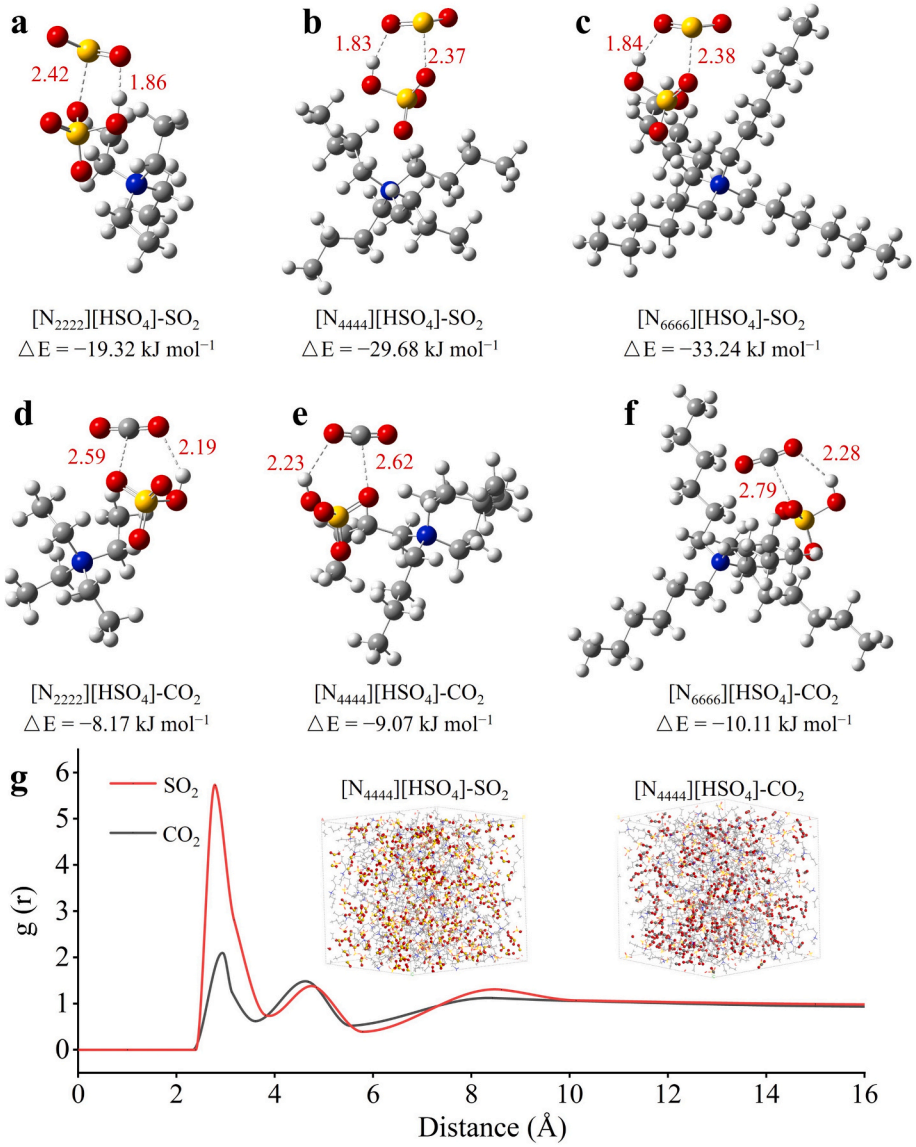

Fig. 8. (a-f) Optimized binding structures of AQA-HSO_4 ILs anion–SO_2/CO_2 intermolecular distances (Å, gray dashed lines) and interaction energies (△E, kJ mol^{-1}); (g) RDFs for HSO_4(O)–SO_2(S) and HSO_4(O)–CO_2(C) in $[N_{4444}][HSO_4]$ obtained from MD simulations.

desorption stage at room temperature, implying the excellent reversibility and facile recyclability of $[N_{4444}][HSO_4]$ IL system. Overall, the combination of the above-mentioned high absorption capacity, remarkable SO_2/CO_2 selectivity, and efficient regenerability supports the significant potential of $[N_{4444}][HSO_4]$ for long-term and stable operation under industrial conditions.

4. Conclusions

In summary, we successfully designed and synthesized a series of AQA-HSO_4 ILs that achieve highly selective SO_2 separation through a gas-triggered, reversible solid–liquid phase transition. By rationally tuning the alkyl chain length on the quaternary ammonium cation, we demonstrated that the local interaction environment can be modulated to optimize hydrogen bonding, Coulombic interactions, and Van der Waals forces between SO_2 and $[HSO_4]^-$ anion. Among the tested AQA-HSO_4 absorbents, $[N_{4444}][HSO_4]$ exhibits superior SO_2/CO_2 selectivity (855) and uptake capacity (7.1 mmol g^{-1}) at 293.2 K and 100 kPa. Meanwhile, this IL absorbent effectively overcame mass transfer limitations via its rapid phase transition, capturing 67% of its total SO_2 capacity within 5 min. Moreover, DFT, COSMOtherm and MD simulations results support that the interaction energy of $[N_{4444}][HSO_4]$ + SO_2 system is more negative than that of $[N_{4444}][HSO_4]$ + CO_2, which is consistent with the observed gas solubility. Furthermore, $[N_{4444}][HSO_4]$ showed outstanding practical reusability, maintaining structural integrity and negligible capacity loss (<0.1%) over 20 absorption–desorption cycles. Crucially, the system can be fully regenerated at room temperature solely by depressurization to ~20 kPa, offering a low-energy pathway for high-purity gas separation. Therefore, this work demonstrates that rational tuning of intermolecular forces in ionic liquids enables gas-triggered phase transitions, creating absorbents that combine high purity gas separation with facile regenerability. We believe that this strategy provides a promising pathway toward the development of next-generation absorbents for diverse challenging and energy-demanding separation processes.

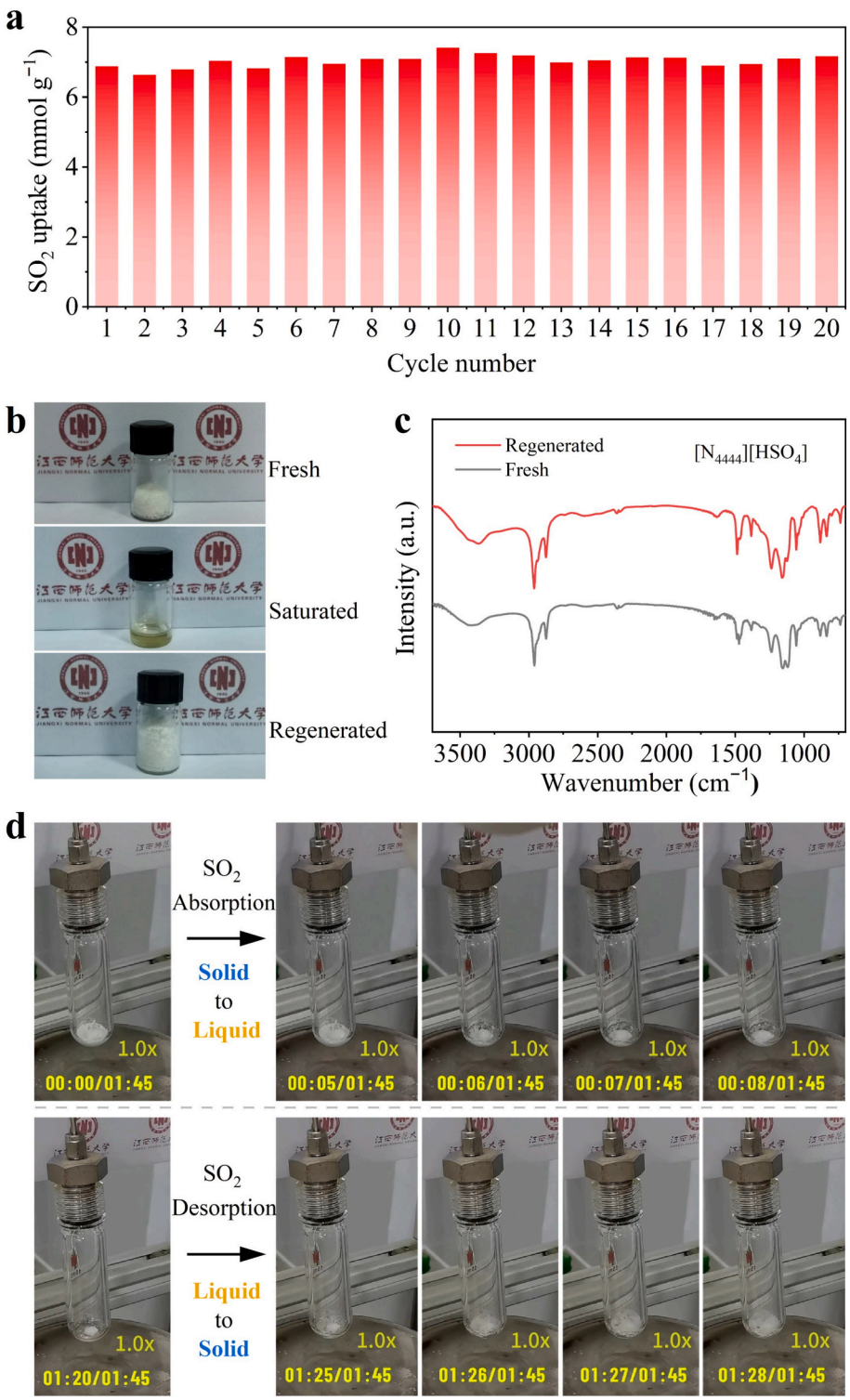

Fig. 9. (a) Reusability of $[N_{4444}][HSO_4]$ for SO_2 uptake at 293.2 K and 100 kPa; (b) photographs of $[N_{4444}][HSO_4]$ in fresh, saturated, and regenerated states; (c) FT-IR spectra of fresh and recycled $[N_{4444}][HSO_4]$; (d) time-lapse snapshots of the reversible solid–liquid phase transition during absorption–desorption by $[N_{4444}][HSO_4]$.

CRediT authorship contribution statement

Xiao-Ya Wang: Investigation, Formal analysis. **Wen-Qiang Gong:** Investigation, Formal analysis. **Fei-Feng Mao:** Visualization, Investigation. **Wei Hui:** Writing – original draft, Supervision, Resources, Funding acquisition, Conceptualization, Methodology, Writing – review & editing. **Xian-Lu Wu:** Investigation. **Tiao Zhang:** Formal analysis, Data curation. **Yan Zhou:** Investigation. **Jia-Yin Zhang:** Validation. **Duan-Jian Tao:** Resources, Project administration, Methodology, Funding acquisition, Writing – review & editing.

Declaration of competing interest

The authors declare that they have no known competing financial interests or personal relationships that could have appeared to influence the work reported in this paper.

Acknowledgments

We gratefully thank the National Natural Science Foundations of China (22378178), the Natural Science Foundations of Jiangxi Province (20242BAB20111), the Natural Science Foundation of Ji'an (20244-018658) for financial support.

Appendix A. Supplementary data

Supplementary data to this article can be found online at https://doi.org/10.1016/j.ces.2026.123635.

Data availability

Data will be made available on request.

References

Bora, K., Özge, Y., Hasan, Y., 2025. Emergency admissions due to respiratory problems in Children change with extend of air pollution. J. Pediatr. Res. 12, 83–89. https://doi.org/10.4274/jpr.galenos.2025.93357.

Chen, J.H., Jiang, H.Y., Gong, W.Q., Hui, W., Zhang, X.L., Sun, M.S., Zhang, J.Y., Cai, D. D., Tao, D.J., 2025. Acetic acid-assisted synthesis of Zr-based metal organic framework for rapid and efficient low-concentration ammonia adsorption. Chem. Eng. J. 525, 170580. https://doi.org/10.1016/j.cej.2025.170580.

Chen, M.S., Li, M.J., Zhang, L., Liu, X.M., Zhang, F., Wu, Y.T., 2022. Intensification of amino acid ionic liquids with different additives for CO_2 capture. ACS Sustain. Chem. Eng. 10, 12082–12089. https://doi.org/10.1021/acssuschemeng.2c00801.

Córdoba, P., 2015. Status of flue gas desulphurisation (FGD) systems from coal-fired power plants: Overview of the physic-chemical control processes of wet limestone FGDs. Fuel 144, 274–286. https://doi.org/10.1016/j.fuel.2014.12.065.

Cui, G.K., Liu, J.X., Lyu, S.Z., Wang, H.Y., Li, Z.Y., Wang, J.J., 2019. Efficient and reversible SO_2 absorption by environmentally friendly task-specific deep eutectic solvents of PPZBr + Gly. ACS Sustain. Chem. Eng. 7, 14236–14246. https://doi.org/10.1021/acssuschemeng.9b03245.

Deng, D.S., Han, G.Q., Jiang, Y.T., 2015. Investigation of a deep eutectic solvent formed by levulinic acid with quaternary ammonium salt as an efficient SO_2 absorbent. New J. Chem. 39, 8158–8164. https://doi.org/10.1039/C5NJ01629K.

Deng, D.S., Liu, X.B., Gao, B., 2017. Physicochemical properties and investigation of azole-based deep eutectic solvents as efficient and reversible SO_2 absorbents. Ind. Eng. Chem. Res. 56, 13850–13856. https://doi.org/10.1021/acs.iecr.7b02478.

Fang, G.W., Li, Z.M., Li, J.F., Cai, D.D., Xiong, Y.J., Zhou, Y., Hui, W., Tao, D.J., 2025. Waste lignosulfonate upcycling towards durable and efficient pelletized adsorbents for diluted NH_3 adsorption. Chem. Eng. J. 507, 160639. https://doi.org/10.1016/j.cej.2025.160639.

Guo, X., Wang, J.L., 2019. A general kinetic model for adsorption: Theoretical analysis and modeling. J. Mol. Liq. 288, 111100. https://doi.org/10.1016/j.molliq.2019.111100.

Heldebrant, D.J., Koech, P.K., Yonker, C.R., 2010. A reversible zwitterionic SO_2-binding organic liquid. Energy Environ. Sci. 3, 111–113. https://doi.org/10.1039/B916550A.

Huang, K., Wu, Y.T., Hu, X.B., 2016. Effect of alkalinity on absorption capacity and selectivity of SO_2 and H_2S over CO_2: Substituted benzoate-based ionic liquids as the study platform. Chem. Eng. J. 297, 265–276. https://doi.org/10.1016/j.cej.2016.03.142.

Hui, W., Wang, X., Wang, X.Y., Mao, F.F., Zhang, T., Zhou, Y., Zhang, J.Y., Tao, D.J., 2025. Tuning cationic structures in ionic liquids for enhanced sulfur dioxide absorption-desorption and mass transfer efficiency. Green. Chem. Eng. https://doi.org/10.1016/j.gce.2025.12.005.

Iliuta, I., Hasib-ur-Rahman, M., Larachi, F., 2014. CO_2 absorption in diethanolamine/ionic liquid emulsions–chemical kinetics and mass transfer study. Chem. Eng. J. 240, 16–23. https://doi.org/10.1016/j.cej.2013.11.063.

Jiang, B., Zhang, H.M., Zhang, L.H., Zhang, N., Huang, Z.H., Chen, Y., Sun, Y.L., Tantai, X.W., 2019. Novel deep eutectic solvents for highly efficient and reversible absorption of SO_2 by preorganization strategy. ACS Sustain. Chem. Eng. 7, 8347–8357. https://doi.org/10.1021/acssuschemeng.8b06822.

Khamizov, R.K., 2020. A pseudo-second order kinetic equation for sorption processes. Russ. J. Phy. Chem. A 94, 171–176. https://doi.org/10.1134/s0036024420010148.

Lee, H.J., Lee, K.I., Kim, M., Suh, Y.W., Kim, H.S., Lee, H., 2016. Diamine-anchored polystyrene resins for reversible SO_2 adsorption. ACS Sustain. Chem. Eng. 4, 2012–2019. https://doi.org/10.1021/acssuschemeng.5b01325.

Lei, Z., Dai, C., Chen, B., 2014. Gas solubility in ionic liquids. Chem. Rev. 114, 1289–1326. https://doi.org/10.1021/cr300497a.

Li, G., Zhao, W., Chai, M., Li, Y., Jia, Q., Chen, Y., 2018. Liquid-liquid phase-change absorption of SO_2 using N, N-dimethylcyclohexylamine as absorbent and liquid paraffin as solvent. J. Hazard. Mater. 360, 89–96. https://doi.org/10.1016/j.jhazmat.2018.07.105.

Li, Z., Li, J., Rong, H., Zuo, J., Yang, X., Xing, Y., Liu, Y., Zhu, G., Zou, X., 2022. SO_2/NO_2 separation driven by NO_2 dimerization on SSZ-13 zeolite membrane. J. Am. Chem. Soc. 144, 6687–6691. https://doi.org/10.1021/jacs.2c01635.

Liu, X.B., Gao, B., Deng, D.S., 2018. SO_2 absorption/desorption performance of renewable phenol-based deep eutectic solvents. Sep. Sci. Technol. 53, 2150–2158. https://doi.org/10.1080/01496395.2018.1446026.

Lu, T., Chen, F.W., 2012. Multiwfn: A multifunctional wavefunction analyzer. J. Comput. Chem. 33, 580–592. https://doi.org/10.1002/jcc.22885.

Lu, T., Chen, Q., 2022. Independent gradient model based on Hirshfeld partition: A new method for visual study of interactions in chemical systems. J. Comput. Chem. 43, 539–555. https://doi.org/10.1002/jcc.26812.

Ma, L., Watrelot, A.A., Addison, B., Waterhouse, A.L., 2018. Condensed tannin reacts with SO_2 during wine aging, yielding flavan-3-ol sulfonates. J. Agric. Food Chem. 66, 9259–9268. https://doi.org/10.1021/acs.jafc.8b01996.

Ortiz, A., Galán, L.M., Gorri, D., Haan, A.B.D., Ortiz, I., 2010. Kinetics of reactive absorption of propylene in RTIL-Ag+media. Sep. Purif. Technol. 73, 106–113. https://doi.org/10.1016/j.seppur.2010.03.008.

Pan, H.Q., Zhao, J.Q., Yang, L.F., Suo, X., Cui, X.L., Xing, H.B., 2024. Modulating pore microenvironment in a robust ionic porous polymer for efficient propyne/propylene separation. Chem. Eng. Sci. 298, 120413. https://doi.org/10.1016/j.ces.2024.120413.

Qi, Y.F., Hu, X.D., Liu, Y.Z., Sun, D.S., Li, R.H., Zhu, H.T., 2019. Highly efficient and reversible absorption of SO_2 by hydroxyl ammonium ionic liquids at low partial pressure. J. Chem. Technol. Biot. 94, 3325–3332. https://doi.org/10.1002/jctb.6143.

Qian, B., Zhao, J., He, Y., Peng, L., Ge, H., Han, B., 2020. Miniaturized dielectric barrier discharge-molecular emission spectrometer for determination of total sulfur dioxide in food. Food Chem. 317, 126437. https://doi.org/10.1016/j.foodchem.2020.126437.

Sun, S.Y., Niu, Y.X., Xu, Q., Sun, Z.C., Wei, X.H., 2015. Efficient SO_2 absorptions by four kinds of deep eutectic solvents based on choline chloride. Ind. Eng. Chem. Res. 54, 8019–8024. https://doi.org/10.1021/acs.iecr.5b01789.

Tian, Y.N., Wang, Y.Z., Hang, Y., Zhou, D.Q., Hu, X.R., Wang, Q.W., 2025. Decoupling economic growth from industrial SO_2 emissions in China: A two-stage decomposition approach. Chin. J. Popul. Resour. Environ. 23, 49–61. https://doi.org/10.1016/j.cjpre.2025.01.005.

Wang, C.M., Cui, G.K., Luo, X.Y., Xu, Y.J., Li, H.R., Dai, S., 2011. Highly efficient and reversible SO_2 capture by tunable azole-based ionic liquids through multiple-site chemical absorption. J. Am. Chem. Soc. 133, 11916–11919. https://doi.org/10.1021/ja204808h.

Wang, L., Zhu, Y.Q., Ye, Y.R., Ma, J.S., Du, J., 2024. Highly selective capture of sulfur dioxide by low viscosity 1,2,4-triazole+[Emim]Cl deep eutectic solvents. Sep. Purif. Technol. 337, 126198. https://doi.org/10.1016/j.seppur.2023.126198.

Wang, Y., Zhao, W.B., Chai, M.Y., Li, G.M., Jia, Q.M., Chen, Y., 2017. Phase-change absorption of SO_2 by imidazole in organic solvents and conversion of the absorption product in the presence of water and oxygen. Energ. Fuel. 31, 13999–14006. https://doi.org/10.1021/acs.energyfuels.7b02694.

Weigend, F., 2006. Accurate Coulomb-fitting basis sets for H to Rn. PCCP 8, 1057–1065. https://doi.org/10.1039/b515623h.

Weigend, F., Ahlrichs, R., 2005. Balanced basis sets of split valence, triple zeta valence and quadruple zeta valence quality for H to Rn: Design and assessment of accuracy. PCCP 7, 3297–3305. https://doi.org/10.1039/b508541a.

Wu, H., Pan, D.P., Huang, R.T., Hong, G.X., Yang, B., Peng, Z.M., Yang, L.J., 2016. Abatement of fine particle emission by heterogeneous vapor condensation during wet limestone-gypsum flue gas desulfurization. Energ. Fuel. 30, 6103–6109. https://doi.org/10.1021/acs.energyfuels.6b00673.

Wu, W., Han, B., Gao, H., Liu, Z., Jiang, T., Huang, J., 2004. Desulfurization of flue gas: SO_2 absorption by an ionic liquid. Angew. Chem. Int. Ed. Engl. 43, 2415–2417. https://doi.org/10.1002/ange.200353437.

Xie, J.P., Wang, D.L., Liu, L., Shao, T.N., Zhou, H.R., Zhang, D.Q., 2024. An overview of flue gas SO_2 capture technology based on absorbent evaluation and process intensification. Ind. Eng. Chem. Res. 63, 6066–6086. https://doi.org/10.1021/acs.iecr.4c00405.

Xu, S.C., Zhao, W.B., Chai, M.Y., Si, T., Chen, Y., Jia, Q.M., 2019. Development of SO_2 phase change absorption: Viscosity change and component distribution rules. Energ. Fuel. 33, 10029–10038. https://doi.org/10.1021/acs.energyfuels.9b01975.

Yang, D.Z., Hou, M.Q., Ning, H., Ma, J., Kang, X.C., Zhang, J.L., Han, B.X., 2013. Reversible capture of SO_2 through functionalized ionic liquids. ChemSusChem 6, 1191–1195. https://doi.org/10.1002/cssc.201300224.

Zeng, S.J., He, H.Y., Gao, H.S., Zhang, X.P., Wang, J., Huang, Y., Zhang, S.J., 2015. Improving SO_2 capture by tuning functional groups on the cation of pyridinium-based ionic liquids. RSC Adv. 5, 2470–2478. https://doi.org/10.1039/c4ra13469a.

Zhang, J., Lu, T., 2021. Efficient evaluation of electrostatic potential with computerized optimized code. PCCP 23, 20323–20328. https://doi.org/10.1039/d1cp02805g.

Zhang, X.M., Feng, X.i., Li, H., Peng, J., Wu, Y.T., Hu, X.B., 2016. Cyano-containing protic ionic liquids for highly selective absorption of SO_2 from CO_2: Experimental study and theoretical analysis. Ind. Eng. Chem. Res. 55, 11012–11021. https://doi.org/10.1021/acs.iecr.6b02588.

Zhao, W.B., Zhao, Q., Zhang, Z., Liu, J.J., Chen, R., Chen, Y., Chen, J., 2017. Liquid-solid phase-change absorption of acidic gas by polyamine in nonaqueous organic solvent. Fuel 209, 69–75. https://doi.org/10.1016/j.fuel.2017.07.081.

Zhao, Y., Truhlar, D.G., 2007. The M06 suite of density functionals for main group thermochemistry, thermochemical kinetics, noncovalent interactions, excited states, and transition elements: two new functionals and systematic testing of four M06-class functionals and 12 other functionals. Theor. Chem. Acc. 120, 215–241. https://doi.org/10.1007/s00214-007-0310-x.